UCSF
UC San Francisco Previously Published Works

Title
Selective ablation of dental caries using coaxial Co2 (9.3-μm) and near-IR (1880-nm) lasers

Permalink
https://escholarship.org/uc/item/7ft7b5zs

Journal
Lasers in Surgery and Medicine, 51(2)

ISSN
0196-8092

Authors
Chan, Kenneth H
Fried, Daniel

Publication Date
2019-02-01

DOI
10.1002/lsm.23002

Peer reviewed

eScholarship.org Powered by the California Digital Library
University of California

Author Manuscript

Author Manuscript

Author Manuscript

Author Manuscript

HHS Public Access

Author manuscript

Lasers Surg Med. Author manuscript; available in PMC 2022 February 24.

Published in final edited form as:

Lasers Surg Med. 2019 February ; 51(2): 176–184. doi:10.1002/lsm.23002.

Selective Ablation of Dental Caries Using Coaxial CO_2 (9.3-μm) and Near-IR (1880-nm) Lasers

Kenneth H. Chan, **Daniel Fried**

Department of Preventive and Restorative Dental Sciences, University of California, San Francisco, San Francisco 94143-0758, California

Abstract

Objective: The purpose of this study was to determine the feasibility of image-guided laser ablation of demineralization from tooth occlusal surfaces using coaxial near-infrared (NIR) and CO_2 lasers.

Materials and Methods: A CO_2 laser operating at a wavelength of 9.3-μm was combined with a thulium-doped fiber laser operating at 1880-nm for the selective removal of simulated occlusal caries lesions from 10 tooth samples. Serial NIR reflectance images at 1880-nm were used to guide the CO_2 laser for image-guided laser ablation. Polarization-sensitive optical coherence tomography (PS-OCT) was used to assess the initial depth of the lesions before removal and assess the volume of sound and demineralized tissue removed by the CO_2 laser.

Results: PS-OCT scans indicated that roughly ~99% of the lesion was removed by image-guided laser ablation. A mean volume of 0.191-mm^3 or 11.9-μm/voxel of excess enamel was removed during lesion removal.

Conclusion: A co-aligned NIR/CO_2 laser scanning system has great potential for the highly selective removal of dental decay (demineralization).

Keywords

selective laser ablation; carbon dioxide laser; near-IR imaging; optical coherence tomography; dental caries

INTRODUCTION

Despite the many advances in dentistry, dental decay remains the most common chronic disease in children [1]. Greater emphasis is being placed on minimally invasive procedures to preserve healthy tooth structure [2]. A highly selective tool that removes unwanted decay, yet leaves sound enamel intact will markedly reduce the amount of healthy tissue loss that is generally associated with conventional cavity preparations. Overaggressive cavity preparations could lead to pulpitis and consequently require more invasive and expensive

Correspondence to: Daniel Fried, Department of Preventive and Restorative Dental Sciences, University of California, San Francisco, 707 Parnassus Ave. 94143 San Francisco 94143-0758, CA. daniel.fried@ucsf.edu.

Conflict of Interest Disclosures: All authors have completed and submitted the ICMJE Form for Disclosure of Potential Conflicts of Interest and have disclosed the following: None of the authors have potential Conflicts of Interest that need to be disclosed.

Author Manuscript Author Manuscript Author Manuscript Author Manuscript

treatments, particularly tooth extraction or root canal treatment. Additionally, incomplete removal of demineralized carious tissue or cariogenic bacteria in the fissure can harbor an active biofilm and lead toward risk of secondary caries [3–5].

Lasers can be focused to very small spot sizes and are ideally suited for the removal of debris, and demineralization and sterilization of the pits and fissures of the occlusal surface prior to the placement of sealants [6]. CO_2 laser wavelengths at λ = 9.3–9.6-μm coincide with the strongest molecular absorption bands in dental hard tissues due to the phosphate ion in hydroxyapatite [7,8]. Moreover, CO_2 lasers can render the irradiated surface more acid-resistant to prevent future decay [9–16]. Lasers can be operated at high pulse repetition rates and precisely scanned at high speeds using galvanometer based scanners or micro-electromechanical systems (MEMS) [17].

Several imaging approaches have been investigated for guiding the removal of dental decay. Fluorescence has been proposed as a means of guiding caries removal by both laser and mechanical means [18–21]. Increased levels of porphyrins accumulate in dentinal caries lesions due to the high porosity and that fluorescence has been employed for caries detection; the Diagnodent device uses such fluorescence. However, the fluorescence is not specifically associated with cariogenic bacteria since they do not contain porphyrins nor is it correlated with the degree of demineralization. Moreover, the fluorescence is weak and diffuse and poorly suited for precise guidance of the laser. In addition stains can lead to false-positive readings, which is a major problem for fluorescence imaging. However, the highly-conjugated organic molecules associated with staining do not absorb near-infrared (NIR) light at wavelengths longer than 1200-nm [22–26].

Previous studies have established that imaging dental decay using NIR wavelengths coincident with higher water absorption and longer wavelengths yield markedly higher contrast between carious and sound tissue [27,28]. Demineralized tooth surfaces are highly porous producing markedly higher light scattering compared to sound tooth surfaces. NIR light is ideally suited for image-guided laser ablation since the contrast between sound and demineralized enamel is highest at wavelengths longer than 1400-nm and there is no interference from stain [22]. Therefore, using NIR images of teeth to guide the CO_2 laser over areas of demineralization is an ideal approach for selective caries removal. A recent study indicated that even higher contrast of demineralization is obtainable at wavelengths longer than 1700-nm due to the further reduction in the light scattering in sound enamel [29]. In this study, we used NIR light at 1880-nm which yields significantly higher contrast of demineralization than 1450-nm which was previously employed for image-guided ablation [30].

Previous studies established that NIR reflectance images can be used to guide a CO_2 laser for the selective removal of caries lesions on smooth and occlusal surfaces [31,32]. This was accomplished by re-iterating a four-phase process until complete caries removal: taking the NIR reflectance image with an InGaAs camera, segmenting demineralization, generating ablation maps or look-up tables (LUTs) of the caries lesion, and scanning the CO_2 laser over demineralized areas for removal. However this approach had significant limitations, the setup was not integrated and it was challenging to precisely align the path of the CO_2

Author Manuscript Author Manuscript Author Manuscript Author Manuscript

laser with the NIR reflectance images; furthermore, lesion segmentation was performed by manually adjusting a global threshold, which is not ideal. In this new study, we used coaxial CO_2 and NIR lasers to both acquire images of demineralization on the tooth surface and remove it selectively. In addition to greatly reducing the cost of the system since an InGaAs camera is no longer needed, the system eliminates alignment errors since the tooth does not need to be removed from the system for serial NIR imaging. Moreover, light can be used at wavelengths longer than the sensitivity of conventional InGaAs cameras (λ > 1700-nm) where higher contrast is attainable such as 1880-nm.

New lesion detection/segmentation tools were also investigated and developed to accurately identify areas of demineralization on tooth surfaces for subsequent laser ablation. In order to assess the accuracy and selectivity of lesion removal, prior knowledge of the lesion volume is required before removal. Previous studies performed selective removal analysis using histological samples to verify absence of lesion, however new methods for monitoring and evaluating dental caries excavation are readily available. Polarization-sensitive optical coherence tomography (PS-OCT) is capable of measuring the initial depth and volume of the lesions before removal and assessing the volume of sound and demineralized tissue removed [33–35]. By nondestructively scanning the tooth before and after lesion removal, PS-OCT was used to demonstrate that a coaxial NIR/CO_2 image-guided laser ablation system is capable of selectively removing early occlusal surface demineralization with high selectivity.

MATERIALS AND METHODS

Sample Preparation

Ten human teeth with non-carious occlusal surfaces were collected and sterilized with gamma radiation. Tooth occlusal surfaces were abraded using air abrasion with 50-μm glass beads for 20 seconds to remove all stain and debris from the fissures and remove the outermost fluoride rich layers of enamel to facilitate the demineralization of those surfaces. Next, teeth were mounted in black orthodontic acrylic blocks. Samples were stored in a moist environment of 0.1% thymol to maintain tissue hydration and prevent bacterial growth. The outlines of a 4×4 mm window (roughly 50-μm deep) were cut on the occlusal surfaces of each tooth using a CO_2 laser (GSI Lumonics, Impact 2500), operating at a wavelength of 9.3-μm, pulse width of 15-μs, and repetition rate of 5-Hz. These markings served as a reference point to denote the demineralized area. The enamel surrounding the 4×4mm windows was covered with acid resistant varnish. Subsurface artificial lesions with intact surfaces were created within the 4 × 4 mm windows by immersing each tooth into a 50 ml aliquot of a Ca/PO_4/acetate solution containing 2.0 mmol/L calcium, 2.0 mmol/L phosphate, and 0.075 mol/L acetate maintained at pH of 4.5 and incubated for 48 hours at 37°C (see Fig. 1A) [36]. Non-destructive cross-polarized optical coherence tomography (CP-OCT) was used to verify lesion presence and measure the depth of demineralization (lesion depth) that varied between 50 and 150-μm deep (see Fig. 1B).

Author Manuscript Author Manuscript Author Manuscript Author Manuscript

Coaxial NIR/CO_2 Laser System

A diagram of the experimental setup is shown in Figure 2. An air-cooled RF-excited laser prototype, Model DL-500 from Access Laser Co (Everett, WA) operating at a wavelength of 9.3-μm was used with a pulse duration of 25-μs and a pulse repetition rate of ~50-Hz (max rate 500-Hz). The laser energy output was monitored using a power meter EPM 1000, Coherent-Molectron (Santa Clara, CA), and Joulemeter ED-200 from Gentec (Quebec, Canada). The laser beam was focused to a beam diameter of 250-μm using a *f*=100-mm ZnSe scanning lens from II–VI Inc. (Saxonburg, PA). A razor blade was scanned across the beam to determine the diameter ($1/e^2$) of the laser beam. The incident fluence was 31 J/cm^2, which removes ~30-μm of sound enamel per pulse. Computer-controlled XY galvanometers 6200HM series with MicroMax Series 671 from Cambridge Technology, Inc. (Cambridge, MA) were used to scan the CO_2 laser beam over the sample surfaces. An air-actuated fluid spray delivery system consisting of a 780S spray valve, a Valvemate 7040 controller, and a fluid reservoir from EFD, Inc. (East Providence, RI) was used to provide a uniform spray of fine water mist onto the tooth surfaces at 2 ml/min.

In order to acquire reflectance images, 1880-nm NIR light from a thulium-doped fiber laser, Model TLT-5 (IPG Photonics, Oxford, MA) was focused onto the occlusal surface of the sample using the same ZnSe *f*=100-mm lens. Crossed polarizers were placed after the light source and before the detector to remove specular reflection (glare) that interferes with measurements of the lesion contrast. We had intended to acquire the NIR images using the same XY galvanometers used to scan the CO_2 laser however we required images of the entire tooth and the imaging area was limited by the fixed field of view of the our detector. Therefore we scanned the tooth using the mechanical stages for NIR image acquisition. Computer-controlled high-speed stage actuators, UTM150 and 850G, from Newport (Irvine, CA) were used to scan tooth surface across the NIR fiber laser beam with a 50-μm pixel pitch. At each scanned point, backscattered NIR light was collected and averaged over five times using an extended range InGaAs photodetector, PDA10DT (ThorLabs, Newton, NJ) and reconstructed into a 2D 8-bit grayscale reflectance image. Prior to imaging, tooth surfaces were air-dried for 10–20 seconds.

Lesion Segmentation and Removal

The flowchart shown in Figure 3 outlines the steps used for the selective removal of demineralization from tooth surfaces. NIR reflectance images were taken by scanning the tooth across the NIR laser beam and acquiring backscattered signal with the extended-range InGaAs photodetector. These data were rasterized into a NIR image. The lesion segmentation algorithm detects and creates a LUT that maps out lesion areas. LUTs were used to direct the CO_2 laser using galvanometer mirror scanners over demineralized areas. The distance between laser pulses was 50-μm, roughly 1/5 of the 250-μm laser spot diameter. Repeated NIR reflectance images and LUTs were taken and these steps were repeated until the lesion was no longer discriminated by the detection algorithm. All image analysis was carried out using Labview (National Instruments, Austin, TX).

Speckle noise is an inherent concern with narrow band laser imaging. An opening operator (3×3^2) filters out speckle noise by clearing lone pixels while preserving the foreground

Author Manuscript Author Manuscript Author Manuscript Author Manuscript

image and its shape. A lesion segmentation program built using Labview was used to evaluate the intensity of each pixel, which represents the acquired backscattered signal. Highly scattering demineralized surfaces *confer* higher signal or appear brighter in NIR reflectance images, while sound tissues appear dark. Pixel intensities were clustered automatically through an adaptive thresholding method based on Otsu's method (six cluster groups) [37]. This classifies groups of pixels as either sound or demineralized by deriving the optimal pixel intensity threshold of each cluster for the least possible variance.

As the lesion is removed, differentiating the decreasing amount of lesion pixels from an increasing amount of sound tissue pixels becomes challenging. The bimodality between lesion and sound pixels of the image is lost as the lesion and its pixels are removed. This causes ambiguity in defining thresholds for classifying lesion and sound tissue groups. A lesion control or phantom of demineralized tissue pixel intensity is necessary, therefore the initial NIR reflectance image containing demineralization was appended with the newly acquired scanned image to serve as a reference. In order to append these images together, a scattering reference target was scanned along with the sample to represent the maximum signal from scattering so that sequential NIR reflectance images could be normalized and compared with each other. Healthy sound enamel structure outside the artificially generated lesion was imaged to provide a positive control of sound tissue pixel intensity. A LUT was created that demarcated lesion areas for removal by the CO_2 laser.

PS-OCT System

The initial lesion depth, the volume of tissue removed by the laser and the residual demineralization after removal were all assessed using PS-OCT. An all-fiber-based optical coherence domain reflectometry (OCDR) system (time-domain) with polarization maintaining (PM) optical fiber, high-speed piezoelectric fiber-stretchers, and two balanced InGaAs receivers that was designed and fabricated by Optiphase, Inc., Van Nuys, CA was used. This two-channel system was integrated with a broadband superluminescent diode (SLD) Denselight (Jessup, MD) and a high-speed XY-scanning system, Newport ESP 300 controller and 850G-HS stages, for *in vitro* optical coherence tomography (OCT). This system is based on a polarization-sensitive Michelson white light interferometer. The high power (15 mW) polarized SLD source operated at a center wavelength of 1317 nm with a spectral bandwidth full-width at half-maximum (FWHM) of 84 nm. The sample arm was coupled to a fiber-collimator to produce a 6-mm diameter, collimated beam. That beam was focused onto the sample surface using an f=20-mm lens to yield a lateral resolution of approximately 20-μm and an axial resolution of 10-μm in air with a signal to noise ratio greater than 40–50 dB. The PS-OCT system is completely controlled using Labview software. The system is described in greater detail in Refs. [38,39]. Acquired scans are compiled into *b-scan* image files [40]. PS-OCT images consist of two orthogonal images, a co-polarization image with the same polarization as the incident light and a cross-polarization (CP) image with the orthogonal polarization.

Processing of PS-OCT Images and Analysis of Selectivity

Both the co-polarization and CP images were utilized in this study. The co-polarization image was used to assess the volume of tissue ablated. The CP-OCT image was used to

Author Manuscript Author Manuscript Author Manuscript Author Manuscript

assess the initial lesion depth and severity. Strong specular reflection from the tooth surface greatly interferes with the measurement of demineralization near the tooth surface. Use of the CP-OCT image reduces that interference and also increases the contrast between sound and demineralized enamel for more accurate assessment of lesion depth and severity [33,39].

PS-OCT *a-scans* were averaged over five times to reduce speckle noise. Data obtained from the PS-OCT scans were further processed using Matlab software from Mathworks (Natick, MA). A global threshold filter was applied using the mean and four times the standard deviation of the background, which was calculated from the top 200 pixels of the *a-scans*. A 3D anisotropic Gaussian filter based on Law et al. [41] was used to further remove speckle noise. Lee and Rhoades demonstrated that applying a 2D rotating kernel transformation (RKT) to OCT *b-scans* improved differentiation of the cartilage-bone border by suppressing noisy signals while simultaneously keeping the details of critical components [42,43]. Studies have shown that the 2D RKT filter can also be used for detecting dental caries and remineralized surface zones with PS-OCT [35]. However, occlusal lesions have irregular shapes and applying a 2D RKT filter on individual *b-scans* is not appropriate. When a 2D RKT filter is applied to the edge of a lesion, these lesion edge signals are unintentionally filtered out thus underestimating the size of the lesion body. Therefore, we created a 3D RKT (5×5×5 kernel) to fully utilize the 3D dataset and help signals of the lesion and occlusal surface stand out.

PS-OCT segmentation was used to extract surface and lesion volume information. Co-polarization OCT images contain the strong reflections from the tooth surface. Conversely, CP-OCT filters out specular reflection from the surface and picks up the subsurface scattering signals emanating from the lesions. A FWHM growing region edge detector starting at the top of every *a-scan* was used to identify the occlusal surface in CP-OCT images. Lesion detection was based on previous work by Lee et al. [35]. For lesion detection an edge locator was used on each *a-scan* in the CP-OCT images and two passes were employed to detect the two edges of the lesion; the top and base. Each pass starts from the position of the maximum peak intensity and locates the first pixel, for which the intensity value is less than e^{-2} multiplied by the maximum peak intensity. Lesion depth was estimated by measuring the distance between the two edges. 3D volumetric datasets were created based on the lesion and surface segmentation.

Determining the amount of tissue ablated is key to assessing the selectivity of the integrated caries ablation system. A 3D iterative closest point algorithm was used to register the occlusal surface data before and after laser treatment (see Fig. 4). Aligning pre- and post-ablation surface points within the 4×4mm window can cause alignment problems since ablation occurred inside the windows, therefore these data points were cropped out during 3D registration. The 3D registration transformation matrix was applied to the moving data set (post-ablation) and a linear interpolation algorithm was applied to fill in the gaps.

Volumetric PS-OCT data can be translated into *en face* 2D projection images representing the depth and severity of demineralization [27,33]. We have taken the same approach for visualizing ablation depth and lesion depth (shown in Fig. 6A, B, and D). The intensity

Author Manuscript Author Manuscript Author Manuscript Author Manuscript

in these 2D maps represent the depth of tissue removed and the remaining depth of demineralization with respect to its location on the occlusal surface.

Ablation volume was calculated by summation of the height differences between pre-ablation and registered post-ablation surfaces. Lesion segmentation was applied to pre- and post-ablation CP-OCT data to compute the lesion volume before and after automated removal. Comparisons made between the initial lesion and the post-ablative lesion volume and the volume of tissue ablated were used to calculate the amount of sound tissue removed and the lesion volume remaining.

Digital Microscopy

Tooth surfaces were examined after laser irradiation using an optical microscopy/3D surface profilometry system, the VHX-1000 from Keyence (Elmwood, NJ). The VH-Z25 lens with a magnification from 25 to 150× was used. Depth composition digital microscopy images (DCDM) were acquired by capturing serial images of varying depth and reconstructing a depth composition image with all points at optimum focus displayed in a 2D image. Images of the samples were acquired before and after ablation at 25× and 50× magnification.

RESULTS

Demineralized enamel was selectively removed from the 4×4mm windows on the 10 teeth according to the process described in the flowchart in Fig. 3. Sequential point-to-point NIR reflectance images were taken during the ablation process using the NIR fiber laser and the InGaAs detector (Fig. 5A–D). Demineralization appears whiter due to increased scattering and the sound tissue structure appears dark. The mean lesion to sound contrast ratio for the ten sample windows was calculated to be 0.67±0.09. Contrast varies from 0 to 1 with a maximum contrast of 1. Therefore a mean contrast of ~0.7 can be considered extremely high. Lesion detection was performed within the 4×4-mm windows using an adaptive thresholding method (outlined in “Lesion Segmentation and Removal” section). Afterwards, a LUT was created and demarcated lesion areas for laser treatment (Fig. 5E–H). Using the LUTs, the CO_2 laser was scanned over the identified lesion area for removal. As the lesion was removed, areas of high reflectivity within the 4×4mm window diminished until the lesion was no longer detected (Fig. 5).

PS-OCT scans taken before and after selective laser ablation were used to assess caries removal. A 2D ablation depth map (Fig. 6A) was created by the registration and subtraction of the initial and final surfaces from the co-polarization OCT scans. Brighter pixels in these depth maps represent deeper ablation depths. For comparison, the initial 2D lesion depth map (Fig. 6B) displays the lesion depth localized within the 4×4mm lesion area. The distinct shape of the tissue removed (in Fig. 6A) correlates well with the shape of the initial lesion (in Fig. 6B), suggesting that the lesion detection algorithm used for the point-to-point NIR reflectance image matches well with the CP-OCT 2D projection image of the initial lesion depth. CP-OCT images were taken again after treatment with the integrated laser scanning system and previously established CP-OCT lesion detection algorithms indicate that the lesion was removed (Fig. 6D). Visible depth composition digital microscopy (DCDM) images were taken before (Fig. 6C) and after (Fig. 6E) laser treatment also indicate complete

Author Manuscript Author Manuscript Author Manuscript Author Manuscript

removal. The white demineralization is apparent on the visible occlusal surface (Fig. 6C) and it extended a bit beyond the initial laser incisions marking the 4×4mm windows (Fig. 6C red-dashed box). The demineralization within the window is absent in the final image after removal (Fig. 6E).

The sum of the pixels within the 4×4mm windows on the 2D depth maps was calculated to determine the total volume ablated, initial lesion volume, and final lesion volume. The average volume ablated was 0.602-mm^3, whereas the average initial lesion volume was 0.411-mm^3. Thus 0.191-mm^3 of excess sound tissue was removed, which equates to a mean 11.9-μm/voxel of excess enamel removed over the entire 4×4mm window. CP-OCT images taken after laser removal indicate that the average remaining volume of demineralization is 2.02×10^{-5}-mm^3, roughly 99% of the initial lesion was removed using the coaxial NIR/CO_2 laser ablation system.

DISCUSSION

The ultimate objective of this work is to develop an image-guided laser system that can be used for the selective removal of dental caries. In this study, the system removed over 99% of the demineralization with a mean loss of a layer of only 11.9-μm of sound tissue. This degree of depth selectivity likely exceeds what would be achievable with the hand-held dental drill.

Previous lesion detection algorithms relied on the user setting a global threshold to identify lesions [32]. This was not ideal as it subjects the selective caries removal to user judgment and bias. In this study, we used an adaptive thresholding method (Otsu's method) and developed controllable variables for accurately detecting occlusal lesions in a non-biased manner. This method is desirable for automating a selective caries ablation system for future studies, since it does not require user input in between every NIR reflectance image. Although, the selective caries ablation system performed well in removing occlusal demineralization, factors including noise, object size, mean differences, contrast, and variances between the object and background can affect this segmentation technique [44]. More avenues of lesion detection, including machine learning, are to be explored in future.

In previous selective ablation experiments, the CO_2 laser caused surface roughening which caused higher reflectivity in irradiated areas and ultimately led to unnecessary tissue removal [32]. However, in this study, the CO_2 laser did not cause any significant surface roughening that interfered with the NIR reflectance images ("Lesion Segmentation and Removal" section) as indicated in the final visible images (Fig. 6E). This is consistent with previous CO_2 laser studies indicating that there were no significant changes in the contrast of sound enamel at NIR wavelengths after laser irradiation and suggests that the previous surface roughening was likely caused by alignment issues between the CO_2 laser and the NIR reflectance camera [45].

The use of a scanned laser for imaging is a less expensive alternative to using InGaAs cameras for NIR image acquisition. The point-to-point NIR laser scanning system yielded images comparable to ones previously taken with InGaAs cameras. The same scanning

Author Manuscript Author Manuscript Author Manuscript Author Manuscript

system can be used for the NIR and the CO_2 laser. In this study, we used an XY stage to scan the tooth to acquire the NIR images. This was required to scan the entire occlusal surface in addition to a scattering reference (maximum 14×14-mm imaging window). Further integration will be needed for a practical clinical system. A single scanning system will be required for both lasers that can encompass the entire area of the tooth that is fast enough for rapid acquisition of NIR images. Large area MEMS mirrors are available that can handle the relatively low single pulse energies (<20-mJ pulses) utilized in this study. The use of multiple fiberoptic cables is a compact method for collecting and delivering backscattered light to the photodetector and this approach can sample a larger scanning area and acquire signals that may be obstructed by the convoluted occlusal topography. The Access CO_2 laser used for this study is unique in that it is compact and does not require water-cooling which is advantageous for use in the dental clinic. The IPG Photonics NIR fiber laser used for this study will need be replaced with a more compact diode laser or LED source. The next step is to produce a fully integrated CO_2/NIR image guided laser ablation system that is compact enough to be fitted into a dental handpiece. We have produced a fully integrated CO_2 spectrally guided laser system for the selective removal of composite restorations from tooth surfaces and that system is currently being used in a clinical study [34].

A secondary goal of this study was to demonstrate that PS-OCT could be used to assess the lesion volume and measure the volume of tissue ablated. We used a previously established PS-OCT lesion detection program for nondestructively quantifying lesion volume and severity and compared this to a new method of analyzing tissue removed [35]. There were some challenges to overcome in measurement of tissue removal volume. Most noticeably during the 3D OCT registration of the initial and final surfaces, the surrounding edges of the occlusal surface did not align well and produced artifacts within the 2D ablation depth map (Fig. 6A). This can be attributed to slightly different angles during PS-OCT imaging and/or the detection of surface edges prior to 3D registration. However, multiple registrations of different PS-OCT scans of the same tooth demonstrated that this method can be reliably used to quantify tissue volume loss. This same approach can be used to evaluate conventional mechanical dental cavity preparations.

In future studies, micro-computed tomography (μCT) can be used to further evaluate the lesion and tissue removal volume. The primary advantage of using μCT is that lesions of any size can be imaged prior to removal in contrast to OCT that has limited penetration in the tooth. However, in contrast to OCT, μCT cannot be used *in vivo* to assess the volume of tissue removed.

In conclusion, we found that this integrated selective caries ablation system is highly selective in removing demineralization. The correlation between the tissue removed and initial lesion volume demonstrates the high selectivity of this system.

ACKNOWLEDGMENTS

We would like to thank Access Laser Co. for providing the air-cooled RF-excited 9.3-μm CO_2 laser used for these studies and Nathaniel Fried for loan of the IPG photonics TLT-5 thulium-fiber laser. This work was supported by NIH/NIDCR Grants R01-DE019631 and F31-DE026350.

Author Manuscript Author Manuscript Author Manuscript Author Manuscript

Contract grant sponsor:

National Institute of Dental and Craniofacial Research; Contract grant numbers: F31-DE026350, R01-DE19631.

REFERENCES

1. Dye BA, Tan S, Lewis BG, et al. Trends in oral health status, United States, 1988–1994 and 1999–2004. Vital Health Stat 2007;11(248):1–92.
2. Vila Verde A, Ramos MM, Stoneham AM. Benefits in cost and reduced discomfort of new techniques of minimally invasive cavity treatment. J Dent Res 2009;88(4):297–299. [PubMed: 19407147]
3. Fejerskov O, Kidd E. editors. Dental Caries: The Disease and its Clinical Management. Oxford: Blackwell; 2003.
4. Hevinga MA, Opdam NJ, Frencken JE, Bronkhorst EM, Truin GJ. Microleakage and sealant penetration in contaminated carious fissures. J Dent 2007;35(12):909–914. [PubMed: 17961903]
5. Kidd EA. How 'clean' must a cavity be before restoration? Caries Res 2004;38(3):305–313. [PubMed: 15153704]
6. Powell GL, Whisenant BK. Comparison of three lasers for dental instrument sterilization. Lasers Surg Med 1991;11(1): 69–71. [PubMed: 1900093]
7. Duplain G, Boulay R, Belanger PA. Complex index of refraction of dental enamel at CO_2 wavelengths. Appl Optics 1987;26:4447–4451.
8. Zuerlein M, Fried D, Featherstone J, Seka W. Optical properties of dental enamel at 9–11μm derived from time-resolved radiometry. Special Topics IEEE J Quant Elect 1999;5(4):1083–1089.
9. Kuroda S, Fowler BO. Compositional, structural and phase changes in *in vitro* laser-irradiated human tooth enamel. Calcif Tissue Int 1984;36:361–369. [PubMed: 6435835]
10. Fowler B, Kuroda S. Changes in heated and in laser-irradiated human tooth enamel and their probable effects on solubility. Calcif Tissue Int 1986;38:197–208. [PubMed: 3011230]
11. Featherstone JDB, Nelson DGA. Laser effects on dental hard tissue. Adv Dent Res 1987;1(1):21–26. [PubMed: 3125842]
12. Nelson DGA, Jongebloed WL, Featherstone JDB. Laser irradiation of human dental enamel and dentine. NZ Dent J 1986;82:74–77.
13. Featherstone JDB, Barrett-Vespone NA, Fried D, Kant-orowitz Z, Lofthouse J. CO_2 laser inhibition of artificial caries-like lesion progression in dental enamel. J Dent Res 1998;77(6):1397–1403. [PubMed: 9649168]
14. Fried D, Featherstone JD, LeCQ Fan K. Dissolution studies of bovine dental enamel surfaces modified by high-speed scanning ablation with a λ=9.3 μm TEA CO_2 laser. Lasers Surg Med 2006;38(9):837–845. [PubMed: 17044095]
15. Hsu DJ, Darling CL, Lachica MM, Fried D. Nondestructive assessment of the inhibition of enamel demineralization by CO_2 laser treatment using polarization sensitive optical coherence tomography. J Biomed Opt 2008;13(5):054027. [PubMed: 19021407]
16. Chang NN, Jew JM, Simon JC, et al. Influence of multi-wavelength laser irradiation of enamel and dentin surfaces at 0.355, 2.94, and 9.4 mum on surface morphology, permeability, and acid resistance. Lasers Surg Med 2017;49(10): 913–927. [PubMed: 28699676]
17. Nguyen D, Chang K, Hedayatollahnajafi S, et al. High-speed scanning ablation of dental hard tissues with a λ=9.3μm CO_2 laser: Adhesion, mechanical strength, heat accumulation, and peripheral thermal damage. J Biomed Opt 2011;16(7):071410. [PubMed: 21806256]
18. Eberhard J, Bode K, Hedderich J, Jepsen S. Cavity size difference after caries removal by a fluorescence-controlled Er:YAG laser and by conventional bur treatment. Clin Oral Invest 2008;12(4):311–318.
19. Eberhard J, Eisenbeiss AK, Braun A, Hedderich J, Jepsen S. Evaluation of selective caries removal by a fluorescence feedback-controlled Er:YAG laser *in vitro*. Caries Res 2005;39(6):496–504. [PubMed: 16251795]

Author Manuscript Author Manuscript Author Manuscript Author Manuscript

20. Jepsen S, Acil Y, Peschel T, Kargas K, Eberhard J. Biochemical and morphological analysis of dentin following selective caries removal with a fluorescence-controlled Er: YAG laser. Lasers Surg Med 2008;40(5):350–357. [PubMed: 18563782]
21. Fried WA, Chan KH, Fried D, Darling CL. High contrast reflectance imaging of simulated lesions on tooth occlusal surfaces at near-IR wavelengths. Lasers Surg Med 2013; 45(8):533–541. [PubMed: 23857066]
22. Almaz EC, Simon JC, Fried D, Darling CL. Influence of stains on lesion contrast in the pits and fissures of tooth occlusal surfaces from 800–1600-nm. In: Lasers in Dentistry XXII; 2016. Proc. SPIE Vol. 9692 p 0X:1–6.
23. Kleter GA. Discoloration of dental carious lesions (a review). Arch Oral Bio 1998 43:629–632. [PubMed: 9758045]
24. Sarna T, Sealy RC. Photoinduced oxygen consumption in melanin systems. Action spectra and *quantum* yields for eumelanin and synthetic melanin. Photochem Photobiol 1984;39:69–74. [PubMed: 6422483]
25. Fu D, Ye T, Matthews TE, Yurtsever G, Warren WS. Two-color, two-photon, and excited-state absorption microscopy. J Biomed Opt 2007;12(5):054004. [PubMed: 17994892]
26. Simon JC, Kang H, Staninec M, et al. Near-IR and CP-OCT imaging of suspected occlusal caries lesions. Lasers Surg Med 2017;49(3):215–224. [PubMed: 28339115]
27. Simon JC, Chan KH, Darling CL, Fried D. Multispectral near-IR reflectance imaging of simulated early occlusal lesions: Variation of lesion contrast with lesion depth and severity. Lasers Surg Med 2014;46(3):203–215. [PubMed: 24375543]
28. Fried D, Featherstone JDB, Darling CL, Jones RS, Ngao-theppitak P, Buehler CM. Early caries imaging and monitoring with near-IR light. Dent Clin North Am 2005;49(4): 771–794. [PubMed: 16150316]
29. Chan KH, Fried D. Multispectral cross-polarization reflectance measurements suggest high contrast of demineralization on tooth surfaces at wavelengths beyond 1300-nm due to reduced light scattering in sound enamel. J Biomed Opt 2018; 23(6):060501.
30. Chan KH, Fried NM, Fried D. Selective ablation of carious lesions using an integrated near-IR imaging system and a novel 9.3-μm CO_2 Laser In: Lasers in Dentistry XXIV; 2018. Proc. SPIE Vol. 10473 p 0E:1–7.
31. Tao YC, Fried D. Near-infrared image-guided laser ablation of dental decay. Journal of Biomedical Optics 2009;14(5): 054045. [PubMed: 19895146]
32. Tom H, Chan KH, Darling CL, Fried D. Near-IR image-guided laser ablation of demineralization on tooth occlusal surfaces. Lasers Surg Med 2016;48(1):52–61. [PubMed: 26763111]
33. Chan KH, Chan AC, Fried WA, Simon JC, Darling CL, Fried D. Use of 2D images of depth and integrated reflectivity to represent the severity of demineralization in cross-polarization optical coherence tomography. J Biophotonics 2015;8(1–2):36–45. [PubMed: 24307350]
34. Jang AT, Chan KH, Fried D. Automated ablation of dental composite using an IR pulsed laser coupled to a plume emission spectral feedback system. Lasers Surg Med 2017;49(7):658–665. [PubMed: 28467687]
35. Lee RC, Kang H, Darling CL, Fried D. Automated assessment of the remineralization of artificial enamel lesions with polarization-sensitive optical coherence tomography. Biomed Opt Express 2014;5(9):2950–2962. [PubMed: 25401009]
36. Featherstone JDB, Glena R, Shariati M, Shields CP. Dependence of *in vitro* demineralization and remineralization of dental enamel on fluoride concentration. J Dent Res 1990;69:620–625. [PubMed: 2312892]
37. Otsu NA. Threshold selection method from gray-level histograms. IEEE Trans Syst Man Cybern 1979;9(1): 62–66.
38. Bush J, Davis P, Marcus MA. All-Fiber Optic Coherence Domain Interferometric Techniques. In: Fiber Optic Sensor Technology II; 2000. Proc SPIE. Vol. 4204 p 71–80.
39. Fried D, Xie J, Shafi S, Featherstone JDB, Breunig T, Lee CQ. Early detection of dental caries and lesion progression with polarization sensitive optical coherence tomography. J Biomed Optics 2002;7(4):618–627.
40. Brezinski M Optical Coherence Tomography: Principles and Applications. London: Elsevier; 2006.

Author Manuscript Author Manuscript Author Manuscript Author Manuscript

41. Law MW, Chung AC. Efficient implementation for spherical flux computation and its application to vascular segmentation. IEEE Trans Image Process 2009;18(3):596–612. [PubMed: 19211333]
42. Lee YK, Rhodes WT. Nonlinear image processing by a rotating kernel transformation. Opt Lett 1990;15(23):1383–1385. [PubMed: 19771098]
43. Rogowska J, Bryant CM, Brezinski ME. Cartilage thickness measurements from optical coherence tomography. J Opt Soc Am A Opt Image Sci Vis 2003;20(2):357–367. [PubMed: 12570303]
44. Lee SU, Yoon Chung S, Park RH. A comparative performance study of several global thresholding techniques for segmentation. Comput Vision Graphics Image Process 1990;52(2): 171–190.
45. LaMantia NR, Tom H, Chan KH, Simon JC, Darling CL, Fried D. High contrast optical imaging methods for image guided laser ablation of dental caries lesions. In: Lasers in Dentistry XX; 2014. Proc. SPIE Vol. 8929 p 1–7.

Author Manuscript Author Manuscript Author Manuscript Author Manuscript

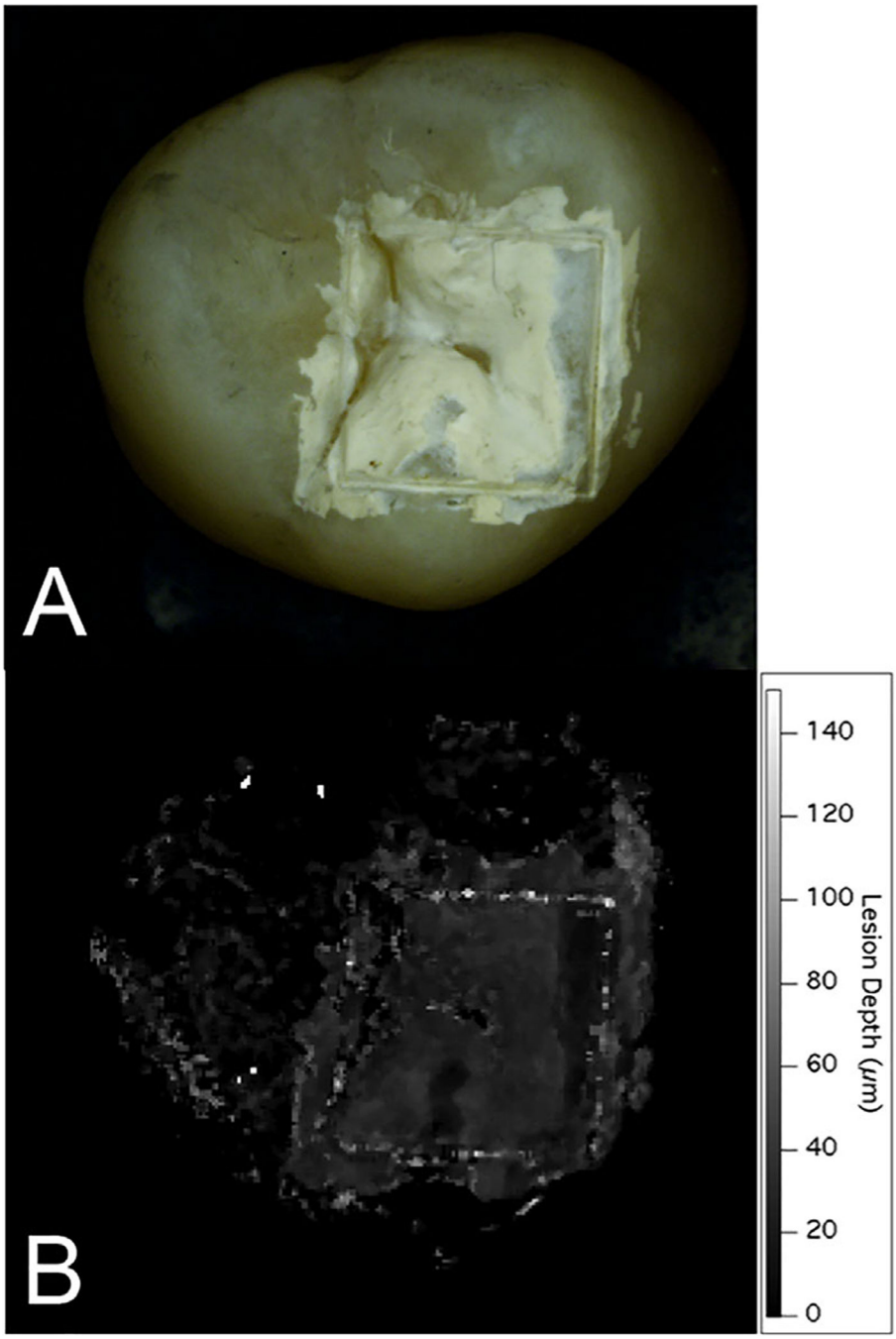

Fig. 1.

(**A**) Depth composition digital microscopy image of one of the 4×4mm windows with demineralization taken at 25× magnification. (**B**) 2D projection image of the lesion depth of the same sample generated from CP-OCT scans.

Author Manuscript Author Manuscript Author Manuscript Author Manuscript

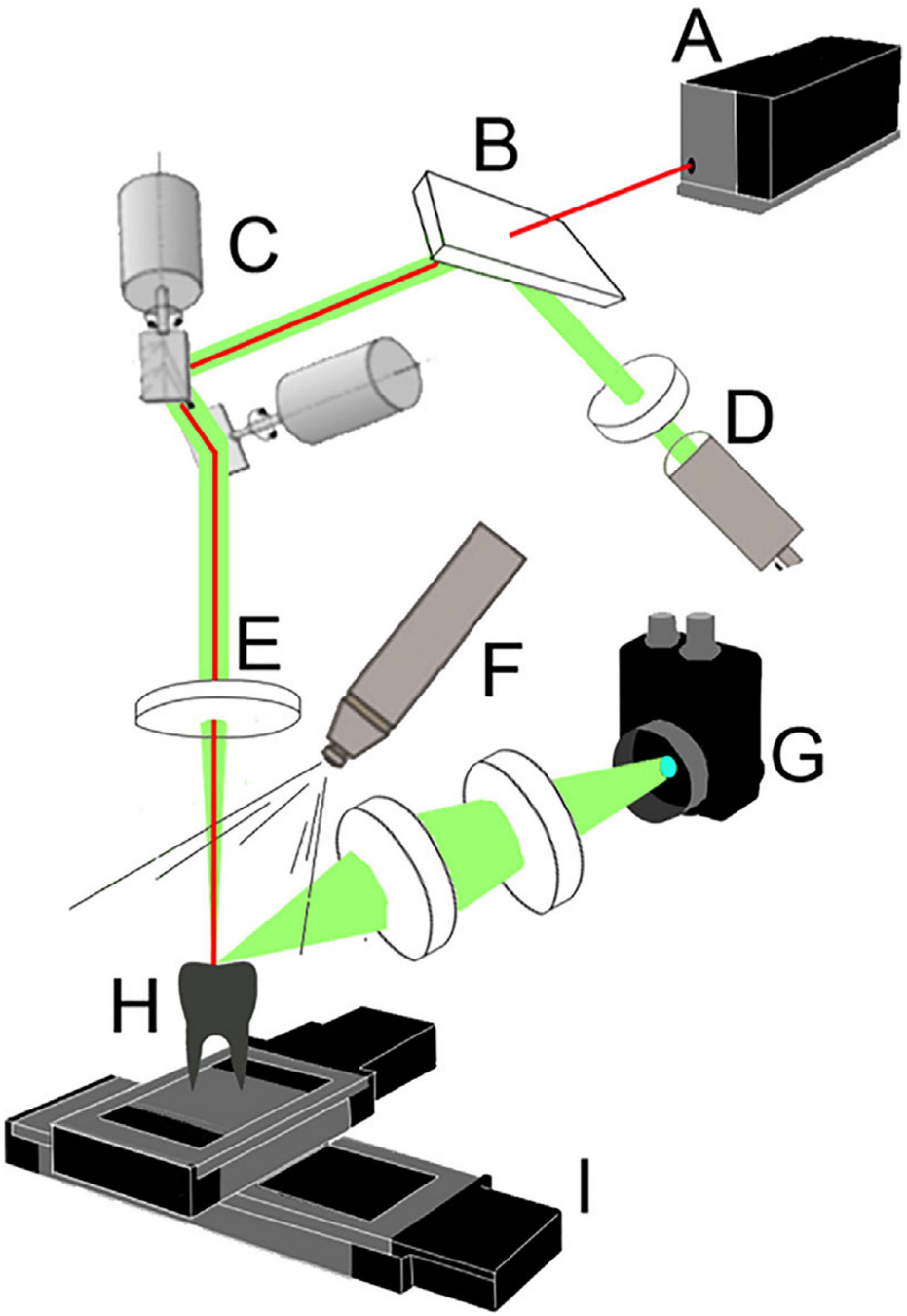

Fig. 2.

Diagram of the NIR/CO_2 laser scanning system with (**A**) CO_2 laser, (**B**) beamsplitter, (**C**) XY galvanometer scanner, (**D**) NIR fiber laser with polarizer; (**E**) ZnSe scanning lens, (**F**) water-spray nozzle, (**G**) InGaAs detector, (**H**) tooth, and (**I**) XY stages.

Author Manuscript Author Manuscript Author Manuscript Author Manuscript

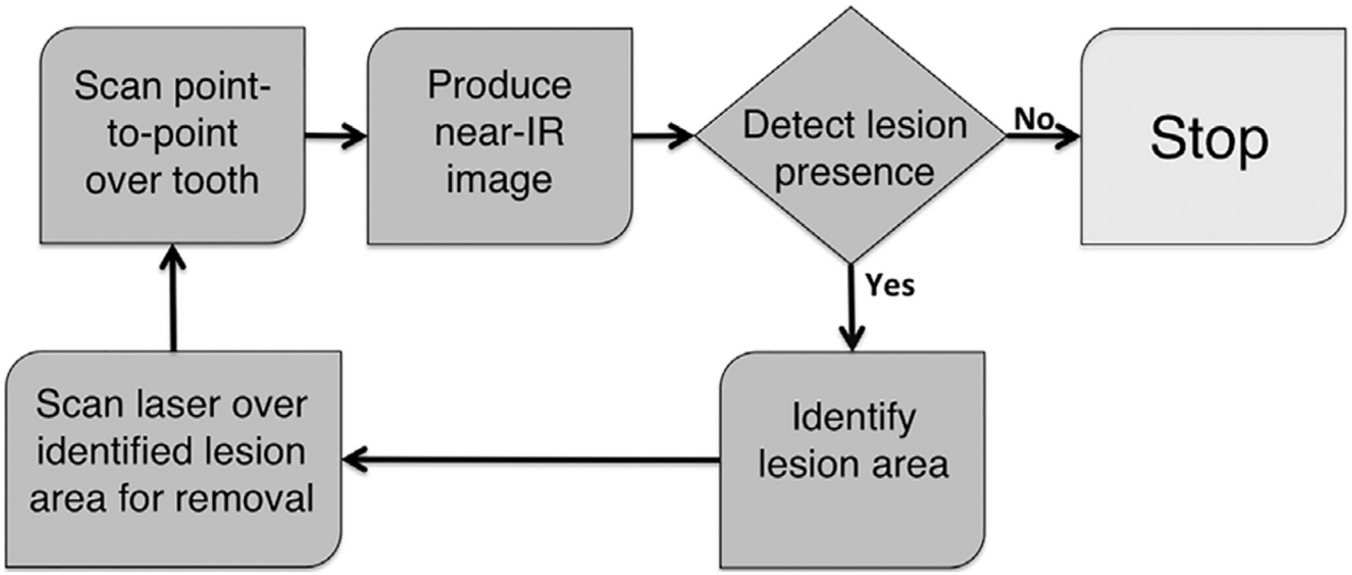

Fig. 3.
Flow-chart of experimental procedures.

Author Manuscript Author Manuscript Author Manuscript Author Manuscript

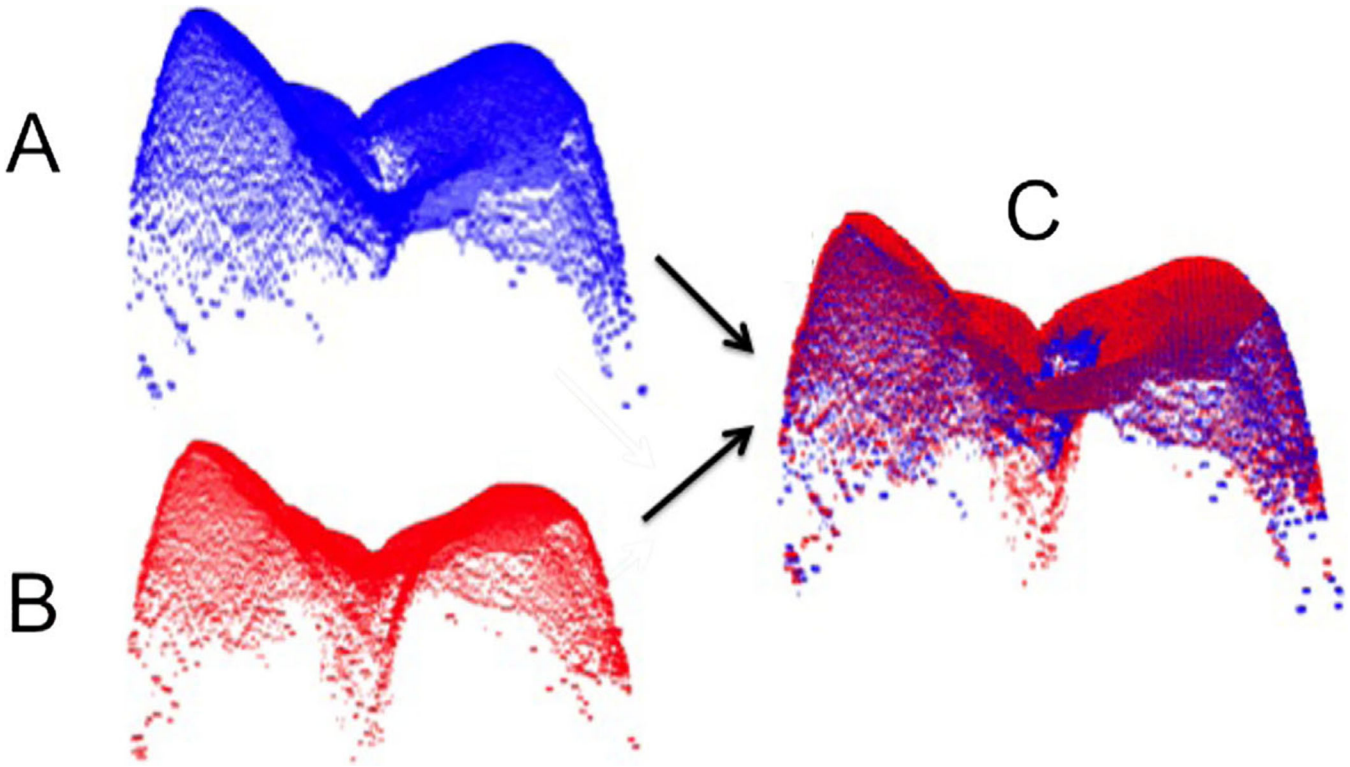

Fig. 4.

3D surfaces imaged with co-polarization OCT. (**A**) 3D preablation surface; (**B**) 3D postablation surface; (**C**) Pre-/post-ablation surface 3D registered to determine volume of tissue removed.

Author Manuscript Author Manuscript Author Manuscript Author Manuscript

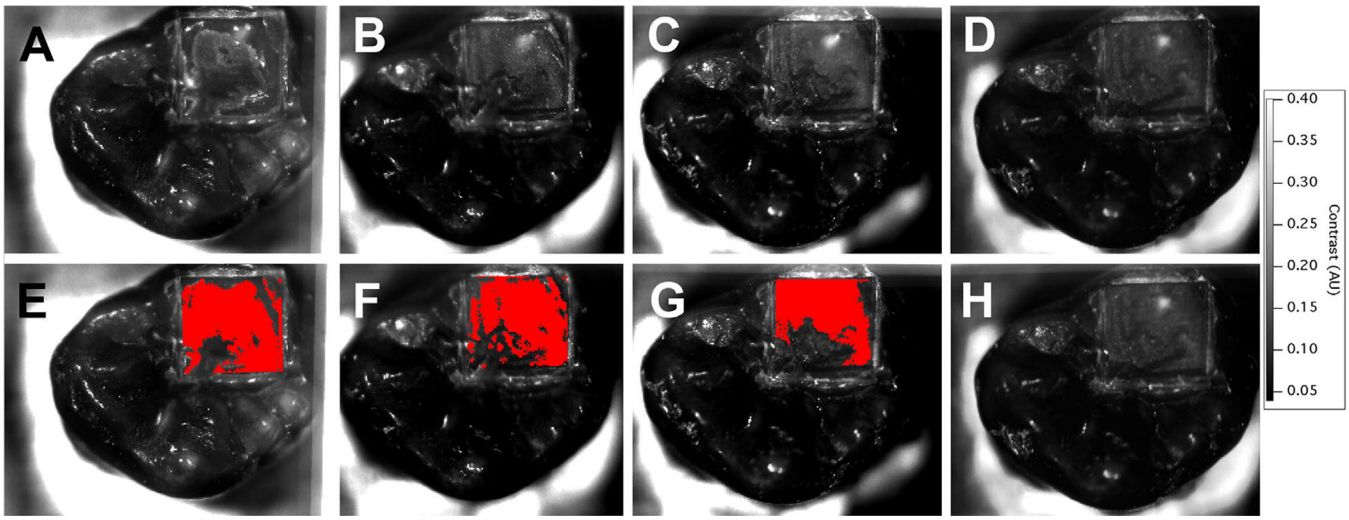

Fig. 5.

(**A**-**D**) Sequential NIR reflectance images generated by the point-to-point NIR scanning system. (**E**-**H**) Look-up-table (in red) overlaid on top of the acquired NIR reflectance images. (**D** and **H**) Final NIR point-to-point reflectance image of the sample. After eight iterations (**H**), demineralization can no longer be detected, suggesting the lesion was completely removed within the 4×4mm window.

Author Manuscript Author Manuscript Author Manuscript Author Manuscript

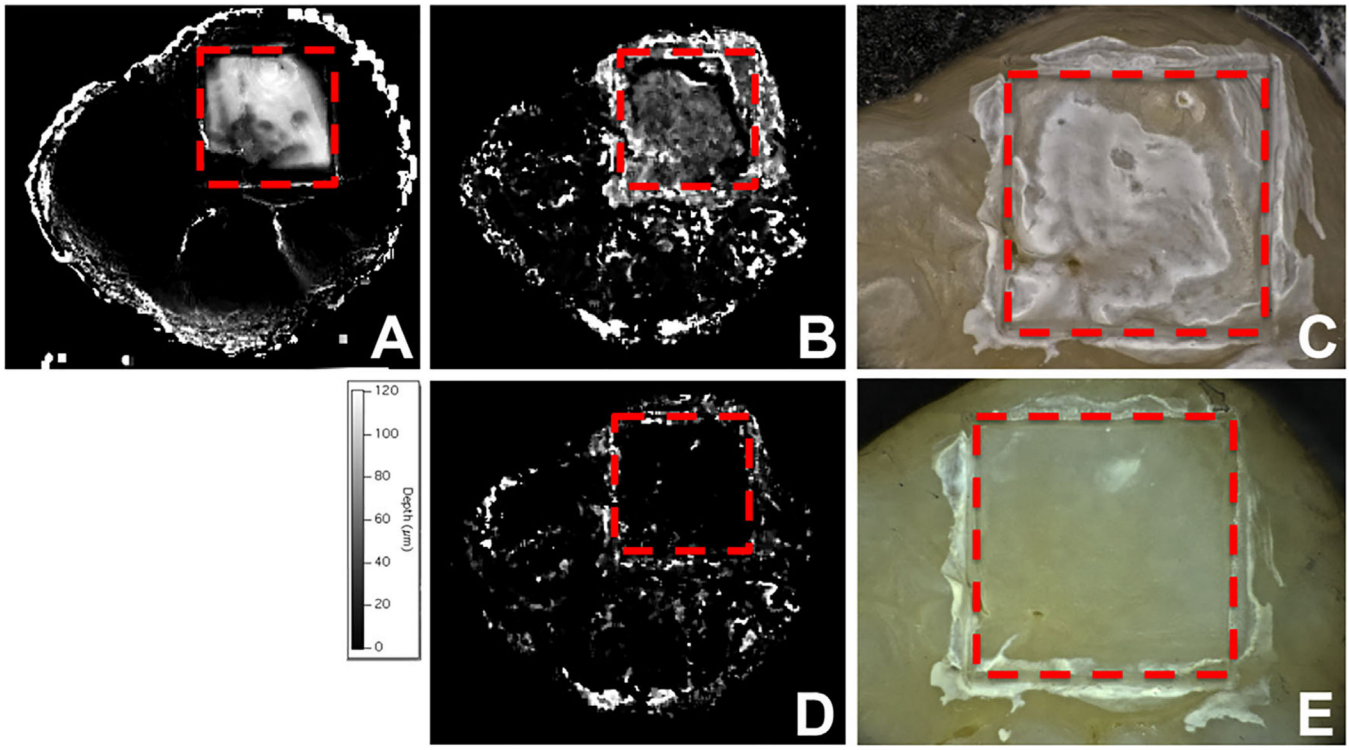

Fig. 6.

(**A**) 2D ablation depth map created by registering and subtracting the initial and final surfaces derived from co-polarization OCT scans showing the area ablated by the laser. (**B**) Initial 2D lesion depth map created from cross-polarized OCT. The area of ablation in (**A**) correlates well with the initial lesion area in (**B**). (C) Depth composition digital microscopy (DCDM) image of the artificially generated lesion before treatment (50×). The white chalky demineralization is visible on the occlusal surface. (**D**) Final 2D lesion depth map taken after selective caries ablation. The absence of bright pixels within the 4×4mm window (red dotted square) indicates the lesion was removed. (**E**) DCDM image of the occlusal surface after selective removal (50×). Note the absence of demineralization within the 4×4mm window (red dotted square).